CO–PROX reactions on copper cerium oxide catalysts prepared by melt infiltration

Xiaobo Li[a], Xian-Yang Quek[b], D.A.J. Michel Ligthart[b], Meiling Guo[a], Yi Zhang[b], Can Li[a], Qihua Yang[a,*], Emiel J.M. Hensen[b,**]

[a] State Key Laboratory of Catalysis, Dalian Institute of Chemical Physics, Chinese Academy of Sciences, 457 Zhongshan Road, Dalian 116023, China
[b] Schuit Institute of Catalysis, Eindhoven University of Technology, P.O. Box 513, 5600 MB Eindhoven, The Netherlands

ARTICLE INFO

ABSTRACT

A series of copper cerium oxide catalysts was prepared by melt infiltration routes using silica hollow spheres (SHS) as the support material. Their catalytic activity in CO oxidation and preferential oxidation of CO in H_2 stream (PROX) strongly depend on the Cu/Ce ratio. Lower ratios resulted in higher activity, indicating that finely dispersed CuO clusters that strongly interact with ceria are the active sites. The highest activity is found for an atomic Cu/Ce ratio of 1/8. The catalysts prepared by melt infiltration are more active than their counterparts prepared by conventional solution impregnation methods. The difference is attributed to the higher proportion of finely dispersed CuO clusters strongly interacting with ceria in the melt infiltrated catalysts.

© 2012 Elsevier B.V. All rights reserved.

1. Introduction

Supported catalysts constitute the most important class of heterogeneous catalytic systems, because of their relevance to improve the conversion and selectivity of a wide variety of industrially important reactions. The main purpose of the support is to increase the dispersion of the active phase, but in many cases the support itself will also contain active sites. A large number of methods developed to prepare supported catalysts, the most common one being solution based impregnation methods, in which water-soluble molecular complexes ranging from simple salts to organometallic complexes, are used as the precursor for the catalytically active phase. As the synthesis method enables control over the catalytic properties of the active phase, the exploration of novel ways to control synthesis is an important research topic [1].

Compared to more commonly applied solution-based methods, such as impregnation, deposition precipitation and ion exchange, solid-state methods have received relatively little attention despite its potential advantages. Mou et al. reported that such catalysts display higher catalytic activity in ethylbenzene dehydrogenation and also slower deactivation compared to impregnated catalysts

[2]. Similar conclusions were reached by Xiao et al. for the selective reduction of NO by propylene [3]. De Jong and co-workers prepared a set of Co/SiO$_2$ catalysts by melt infiltration, which displayed high activity in the Fischer–Tropsch synthesis reaction [4]. Another advantage of solid-state methods is that their preparation is more energy efficient without the problems related to the production of impregnation solutions, purification and recycling. Very often, catalysts comprise more than one active component such as in the case of bimetallic or promoted catalysts. So far, most work on solid-state synthesis methods have focused on supporting a single active component on a carrier material [4]. In principle, as with solution-based methods, one has the possibility to introduce two or more active components in a catalyst *via* solid-state methods, either simultaneously or in a sequential manner.

Ceria-based metal oxide catalysts are good catalysts for a variety of purposes [5]. Among them, copper cerium oxides have been widely studied for the CO preferential oxidation reaction (PROX) [6–8]. Commonly, solution-based methods such as co-precipitation [9], impregnation [10], urea methods [11] and a surfactant method [12] have been used to disperse the copper oxide on ceria or, an alternative is the copper oxide and ceria on an appropriate support material. It is well recognized that the preferential oxidation activity of copper cerium oxide catalysts relates to the special redox properties of sites at the interface between the copper and cerium components. Their presence will significantly depend on the dispersion and, therefore, also on the method of preparation [13–17]. Thus, the copper cerium oxide catalytic system is an interesting

case to investigate the solid-state methods to prepare multicomponent supported catalysts.

Herein, we used melt infiltration routes to prepare copper cerium oxide catalysts on silica hollow spheres (SHS) as the carrier material. The main parameter to be optimized is the Cu/Ce ratio. Their activities were compared against reference samples prepared by conventional impregnation of SHS. The materials were extensively characterized for their physicochemical properties and their activities in oxidation reactions were also determined.

2. Experimental

2.1. Catalyst preparation

2.1.1. Synthesis of silica hollow nanospheres

Silica hollow nanospheres were synthesized according to a modified procedure from literature [18,19]. 5.0 g of the triblock copolymer F127, 5.0 g of 1,3,5-trimethylbenzene (TMB) and 4.35 g of K_2SO_4 were dissolved in 300 mL of deionized water. After stirring the mixture at 13.5 °C for 24 h, TMOS (12.15 g, 80 mmol) was added followed by addition of phenyltrimethoxysilane (3.96 g, 20 mmol). After stirring at 13.5 °C for 24 h, the mixture was transferred into a Teflon-lined autoclave and aged at 100 °C for 24 h. The precipitate was filtered off, washed repeatedly with deionized water and dried at 100 °C. The as-synthesized sample was calcined in air at 550 °C with a rate of 1 °C/min for 10 h to obtain the silica hollow nanospheres.

2.1.2. Synthesis of CuCe(x)/SHS

Copper nitrate salts $Cu(NO_3)_2 \cdot 2.5H_2O$ (Alfa Aesar) (m.p. 114 °C) and ceria nitrate salt $Ce(NO_3)_3 \cdot 6H_2O$ (Alfa Aesar) (m.p. 65 °C) were mixed in a closed vial at 120 °C. After extensive grinding of this mixture with SHS in a mortar, it was placed and sealed in a vial and heated to 120 °C for 24 h. Finally, the solid was calcined in air at 550 °C for 5 h. For these materials the ratio of the sum of weights of $Cu(NO_3)_2 \cdot 2.5H_2O$ and $Ce(NO_3)_3 \cdot 6H_2O$ salts to the weight of the silica support was always unity, while the molar Cu/Ce ratio was varied. Samples are denoted by CuCe(x)/SHS with x the Cu/Ce ratio. A CuCe(1/4)/SHS-IMG catalyst was prepared by dispersing the metal precursors and SHS in 10 mL H_2O, followed by stirring at room temperature and drying at 110 °C. Finally, this solid was calcined in air at 550 °C for 5 h.

2.1.3. HNO3 treatment

An amount of catalyst was dispersed in a solution of 65% HNO_3 for 24 h. The solid sample was retrieved by filtration and copious washing with demineralized water and dried at 110 °C. Samples treated in this way are denoted by the suffix –HNO3.

2.2. Catalyst characterization

The metal loading was determined by inductively coupled plasma atomic emission spectroscopy (ICP-AES) analyses performed on a Goffin Meyvis SpectroCirus[ccd] apparatus. The samples were first dissolved with boiled concentrated sulfuric acid and then added to diluted hydrofluoric acid (HF:H_2O = 1:15) to dissolve silica. Physical parameters were measured with a Micromeritics TriStar 3000 BET apparatus by nitrogen physisorption at −195 °C. XRD analysis was carried out on a well-aligned Bruker D4 Endeavor Diffractometer using Cu Kα radiation (1.54056 Å) with a step size of 0.01° and time per step of 1 s. The lattice parameter of ceria was measured by cell refinement by matching the full pattern using Bruker's Topas software. The XRD measurement and cell refinement were carried out in duplo. Transmission electron micrographs were acquired on a FEI Tecnai 20 transmission electron microscope at an acceleration voltage of 200 kV. Visible Raman
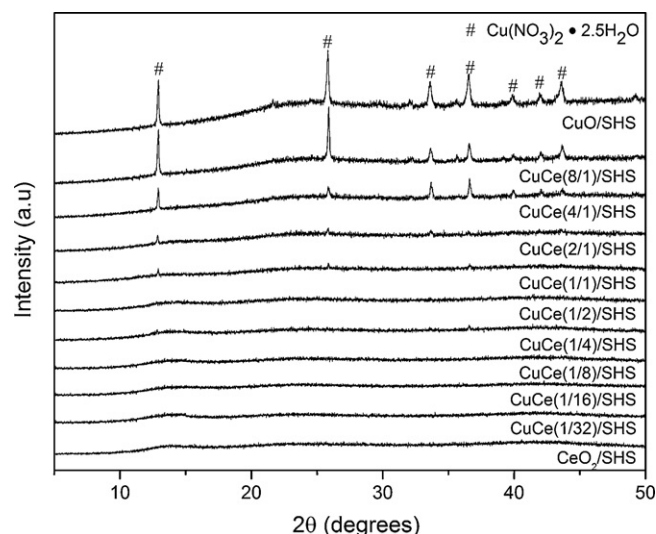

Fig. 1. XRD patterns of CuCe(x)/SHS catalysts after melt infiltration at 120 °C.

spectra were recorded at room temperature on home-built Raman spectrograph with the excitation line at 532 nm. TPR experiments were carried out in a flow apparatus equipped with a fixed-bed reactor, a computer-controlled oven and a thermal conductivity detector. Typically, an amount of catalyst was contained between two quartz wool plugs in a quartz reactor. Prior to TPR, the catalyst was oxidized by exposure to a flowing mixture of 4 vol% O_2 in He while to 300 °C at a rate of 10 °C/min. After the sample was cooled to room temperature in flowing nitrogen, the sample was reduced in 4 vol% H_2 in N_2 at a flow rate of 8 mL/min, while heating from room temperature up to 800 °C at a ramp rate of 10 °C/min. The H_2 signal was calibrated using a CuO/SiO_2 reference catalyst. UV–vis spectra of the solids were measured in diffuse-reflectance mode with an integrated sphere accessory on a Shimadzu UV-2401PC. X-ray photoelectron spectroscopy measurements were carried out on a Thermo Scientific K-Alpha apparatus, equipped with a monochromatic small-spot X-ray source and a 180° double focusing hemispherical analyzer with a 128-channel detector. Spectra were obtained using an aluminium anode (Al Kα = 1486.6 eV) operating at 72 W and a spot size of 400 μm. The background pressure was 2×10^{-9} mbar and during measurement 4×10^{-7} mbar. Binding energy values were referenced to the C 1s peak (284.5 eV).

2.3. Catalytic activity measurements

The catalytic activity in the oxidation of CO in the absence and presence of H_2 was evaluated in a parallel ten-flow microreactor system. The effluent products (CO, CO_2 and O_2) were analyzed by an Interscience CompactGC online gas equipped with Rt-Molsieve 5A/Rt-Q-Bond (TCD), Rt-U-Bond/Rt-Q-Bond (TCD) and Rtx-1 (FID) columns. For CO oxidation, the feed mixture contained 1 vol% CO and 1 vol% O_2 in He at a total flow rate of 400 mL/min. An amount of 30 mg of catalyst was diluted with 100 mg of SiC and contained between two quartz wool plugs in a quartz reactor with an internal diameter of 4 mm. Prior to reaction, the catalysts were pretreated in a flow of 5 vol% O_2 in He at 300 °C for 1 h. The reaction temperature was increased from 40 °C to 300 °C at a rate of 0.6 °C/min. For the preferential oxidation of CO in H_2, the feed mixture contained 1 vol% CO, 1 vol% O_2 and 50 vol% H_2 in He, 400 mL/min in total. The selectivity towards CO_2 was estimated from the oxygen mass balance as follows: Selectivity CO_2 (%) = 0.5 × CO conversion/O_2 conversion.

Table 1
Physicochemical properties of CuCe(x)/SHS catalysts.

Catalyst	CeO$_2$ content[a] (%)	CuO content[a] (%)	(Cu/Ce)[a] ICP	(Cu/Ce)[b] XPS	Surface area (m^2/g)	Pore volume (cm^3/g)	d_{CeO_2}[c] (nm)	Lattice parameter[d] (Å)
CuCe(8/1)/SHS	4.9	20.3	8.17	4.37	266	0.87	–	–
CuCe(4/1)/SHS	7.9	16.0	3.98	1.82	288	0.83	4.5	5.426
CuCe(2/1)/SHS	11.8	11.9	1.98	1.26	275	0.78	4.4	5.418
CuCe(1/1)/SHS	16.1	8.0	0.98	1.10	272	0.73	5.1	5.422
CuCe(1/2)/SHS	21.3	5.4	0.50	0.66	250	0.70	5.2	5.415
CuCe(1/4)/SHS	23.0 (23.1)	2.9 (1.48)	0.25 (0.126)	0.41 (0.115)	260	0.71	5.8	5.409
CuCe(1/8)/SHS	25.3 (23.1)	1.6 (0.94)	0.128 (0.080)	0.260 (0.081)	276	0.76	6.0	5.411
CuCe(1/16)/SHS	28.3	0.86	0.060	0.083	279	0.77	6.1	5.413
CuCe(1/32)/SHS	24.8	0.39	0.031	0.042	274	0.80	6.4	5.410
CuCe(1/4)/SHS-IMG	21.6 (21.7)	2.9 (2.0)	0.26 (0.188)	0.25 (0.136)	298	0.99	6.6	5.400

[a] Measured by ICP-AES; values between brackets after HNO$_3$ treatment.
[b] Measured by XPS; values between brackets after HNO$_3$ treatment.
[c] Ceria particle size estimated by application of the Scherrer equation on XRD data.
[d] Lattice parameter of CeO$_2$/SHS is 5.407 Å.

3. Results and discussion

3.1. Characterization of CuCe(x)/SHS

The SHS support was measured to be surface area 538 m^2/g and pore volume 2.3 cm^3/g [18]. Fig. 1 shows the XRD patterns of the CuCe(x)/SHS composites after melt infiltration at 120 °C. The XRD data show that this method is able to disperse the precursor salts efficiently in the pores of the SHS when Cu/Ce < 1. At low Cu content (Cu/Ce < 1), the typical XRD reflections of the precursor metal salts are not observed. This points to their high dispersion in the pores of the support and possibly their amorphous nature [4,20]. At a Cu/Ce ratio of 1, the XRD pattern of copper nitrate salt is weakly discerned. The pattern becomes more obvious and the intensity increases with a further increase of the Cu content. This could correspond to an increasing amount of extraporous copper nitrate salts. The XRD patterns of these samples after calcination at 550 °C in air are given in Fig. 2. The presence of CeO$_2$ is obvious in all of the samples. In accordance with their precursors, no crystalline copper phases are observed in the calcined CuCe(x)/SHS composites as long as the Cu/Ce ratio is kept below 1/4. This implies that no extensive sintering takes place during the copper nitrate conversion into copper oxide. At a ratio of 1/4, very weak patterns of CuO were observed, indicating the presence of CuO crystallites. Their presence becomes more obvious with a further increase of the Cu content. By application of the Scherrer equation, we find that the ceria particle size slightly increases with the Ce content of the samples (Table 1). The finding that the ceria particle size remains relatively small despite the high Ce content for CuCe(8/1)/SHS implies that the growth of ceria is limited by its inclusion in the hollow spheres. The right panel of Fig. 2 shows the lattice parameter of CeO$_2$ variation as a function of the Cu/Ce ratio. Care should be taken with the accuracy of the lattice parameter, especially concerning the absolute value [21]. The lattice parameter of all CuCe(x)/SHS catalysts was higher than that of CeO$_2$/SHS (Cu/Ce = 0), irrespective of the Cu content (Table 1). The increase of the lattice parameter is the result of the presence of oxygen vacancies [22]. Cu-containing CeO$_2$/SHS samples contain more of such vacancies than CeO$_2$/SHS. From Fig. 2 it is seen that the lattice parameter initially increases up to a Cu/Ce ratio of 1/16, then decreases again until Cu/Ce = 1/4 and then strongly increases with the Cu content. The decrease of the lattice parameter going from Cu/Ce ratios of 1/16 to 1/4 indicates that the lattice contraction due to substitution of Ce by Cu dominates over the opposing lattice expansion resulting from oxygen vacancy
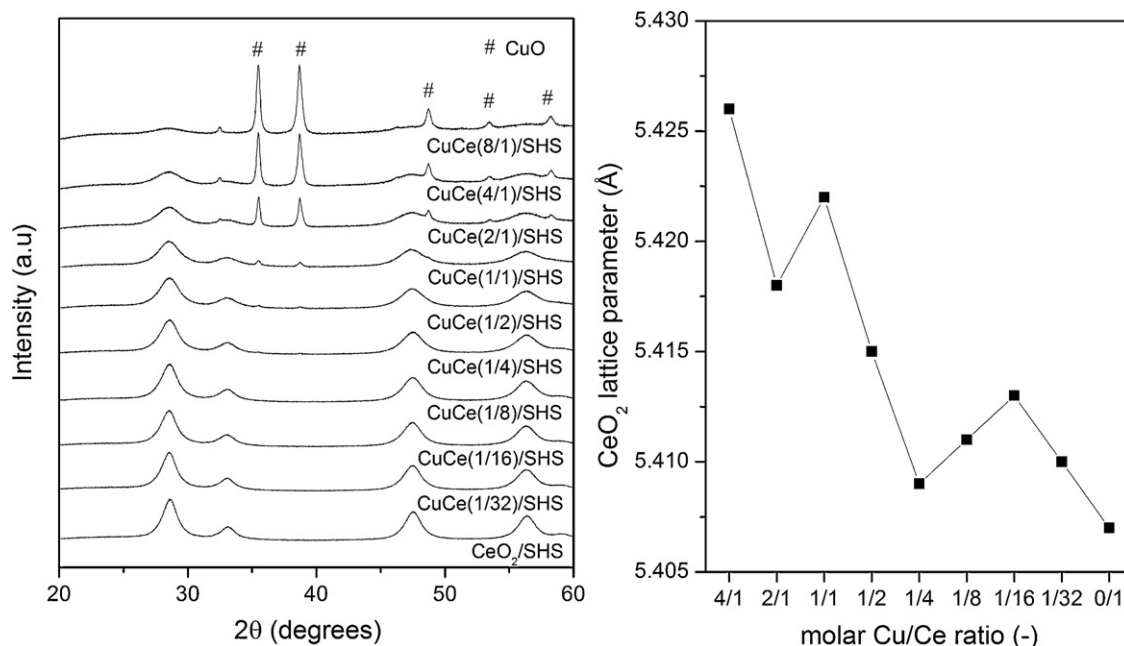
Fig. 2. XRD patterns of CuCe(x)/SHS catalysts after calcination (left panel) and CeO$_2$ lattice parameter as a function of the molar Cu/Ce ratio (right panel).
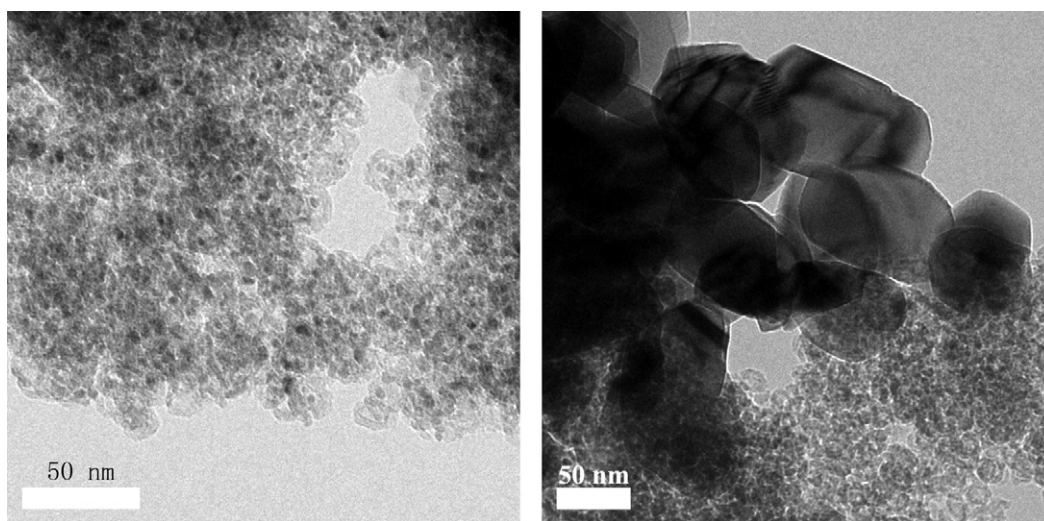
Fig. 3. TEM images of CuCe(1/4)/SHS (left) and CuCe(8/1)/SHS (right).

formation. The substitution effect is related to the smaller size of Cu^{2+} ions (0.87 Å) compared to Ce^{4+} ions (0.97 Å) [11]. The increase of the lattice parameter with a further increase of the Cu/Ce ratio correlates inversely with the ceria particle size as reported before [23].

As the pronounced XRD reflections of copper oxide are only observed for the samples that initially contained large copper nitrate crystallites, it may be inferred that the bulk CuO particles are formed from the extraporous copper precursors due to inefficient infiltration at high Cu content. The samples with a relatively low Cu content contain two types of Cu species [24], namely (i) Cu in a solid solution in ceria and (ii) highly dispersed CuO species. The proportion and size of the latter will increase with the Cu content up to the point where obvious bulk CuO is observed in the patterns (CuCe(1/1)/SHS). Fig. 3 shows a representative TEM image of calcined CuCe(1/4)/SHS and CuCe(8/1)/SHS. The observed yolk-shell structure for CuCe(1/4)/SHS supports the above conclusion that melt infiltration leads to an efficient dispersion of copper and cerium nitrate salts in the silica hollow spheres. The micrographs for CuCe(8/1)/SHS clearly show the presence of very large crystallites of CuO, in agreement with analysis of the XRD patterns. It has been verified that for all Cu/Ce ratios the total salt volume is lower than the pore volume of SHS. No XRD signals of CuO were observed for the CuCe(1/4)/SHS-IMG samples prepared by solution impregnation method (data not shown). The ceria particle sizes of CuCe(1/4)/SHS-IMG is similar to the values obtained for the SHS samples obtained by melt infiltration (Table 1). Compared to CuCe(1/4)/SHS, the sample prepared by the solution-impregnation method exhibits a lattice parameter, which is even lower than that of CeO_2/SHS. A tentative explanation for this is a higher propensity towards the formation of $Cu_xCe_{1-x}O_2$ causing a significant influence of lattice contraction due to substitution. These results point to a strong influence of the preparation method on the extent of interaction between copper and cerium components. The textural properties of the samples as determined by nitrogen physisorption are also collected in Table 1. All of the samples have a rather similar surface area and pore volume. This also holds for CuCe(1/4)/SHS-IMG. The isotherms exhibit two capillary condensation steps, similar to that of SHS, which is typical for hollow nanospheres with microwindows on their shell [19].

Raman spectra of the various samples are shown in Fig. 4. All samples show a main band around $460 \, cm^{-1}$ which has been related to the F_{2g} vibrational mode, characteristic of the cubic fluorite structure of CeO_2 [25,26]. It is attributed to a symmetric breathing mode of oxygen atoms of the CeO_8 unit of the ceria lattice. The broad peak between 520 and $650 \, cm^{-1}$ has been attributed to the oxygen vacancies [25,26]. It is also observed that the characteristic F_{2g} vibrational mode is shifted to lower frequencies and broadened with an increase of the Cu/Ce ratio. These observations can be explained by the combined effects of inhomogeneous strain and phonon confinement related to the presence of reduced states of cerium and smaller CeO_2 units with increasing Cu content [26–28]. The results of Raman spectroscopy are in good agreement with XRD analysis on variation of the particles size with Cu content. The ratio between the areas of 520–650 and $460 \, cm^{-1}$ Raman bands has been related to the concentration of oxygen vacancies in the materials. The higher the ratio, the higher the number of oxygen vacancies [25,26]. Fig. 4 shows the ratio of these areas as a function of the Cu/Ce ratio. It is inferred from these data that the density of oxygen vacancies of the CuCe(x)/SHS catalysts are all higher than that of the pure CeO_2/SHS sample. The density increases with increasing Cu/Ce ratio. This trend is understood in terms of
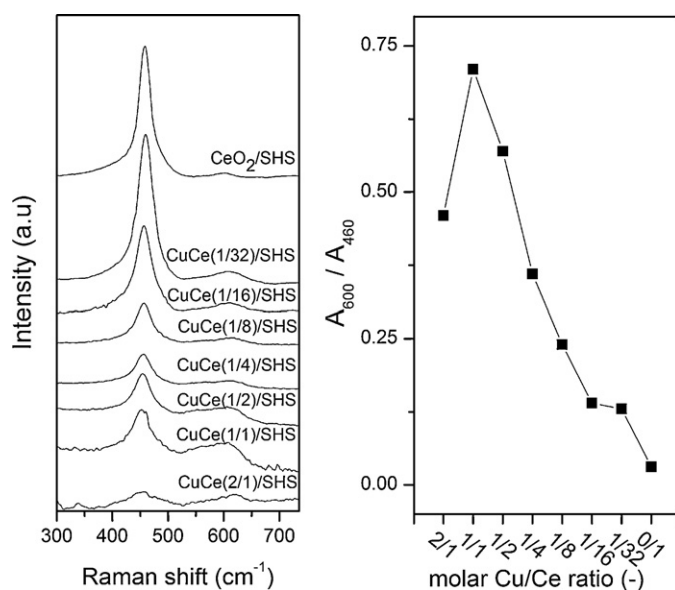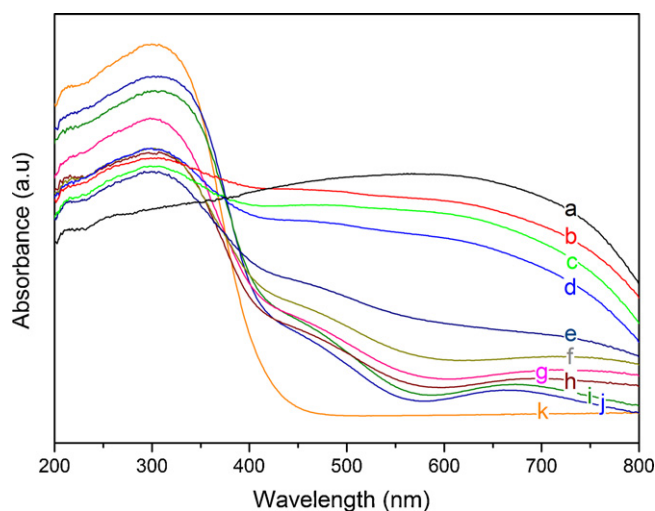

Fig. 4. Raman spectra of CuCe(x)/SHS catalysts (left panel) using 532 nm laser and areas ratio between band 520–650 cm^{-1} (A_{600}) and 460 cm^{-1} (A_{460}) as a function of the molar Cu/Ce ratio (right panel).
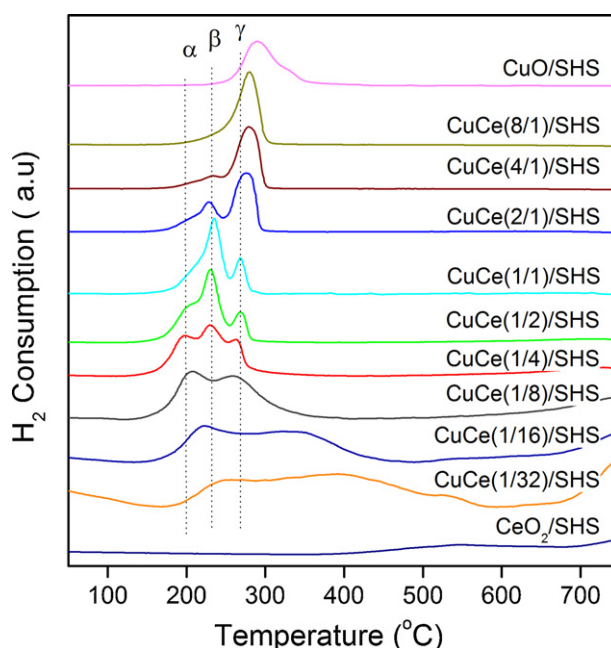
Fig. 5. UV–vis spectra of CuCe(x)/SHS catalysts: (a) CuO/SHS, (b) CuCe(8/1)/SHS, (c) CuCe(4/1)/SHS, (d) CuCe(2/1)/SHS, (e) CuCe(1/1)/SHS, (f) CuCe(1/2)/SHS, (g) CuCe(1/4)/SHS, (h) CuCe(1/8)/SHS, (i) CuCe(1/16)/SHS, (j) CuCe(1/32)/SHS and (k) CeO₂/SHS.

Fig. 6. H₂-TPR profiles of CuCe(x)/SHS catalysts.

keeping charge neutrality when the $Cu_xCe_{1-x}O_2$ solid solution is formed in which Ce^{4+} ions are replaced by Cu^{2+} ions. Besides, the density of oxygen vacancies of nanoscale ceria is related to the particle size. Earlier, it has been observed that the number of oxygen vacancies increases with a decrease of the ceria particle size [23,28].

The UV–vis spectra of the set of CuCe(x)/SHS materials are given in Fig. 5. Compared to CuO/SHS, the ceria-containing samples contain a oxygen-to-Ce^{4+} charge-transfer band and an interband transition around 271 and 347 nm, respectively [29]. The samples with Cu/Ce > 1 exhibit a strong and broad absorption band around 700 nm due to the d–d transition of Cu^{2+} in octahedral symmetry. This is related to the presence of bulk CuO as discussed before [30]. At lower Cu content, this band becomes less broad and shifts to higher wavelengths. It is assigned to d–d transitions of Cu^{2+} in distorted octahedral symmetry and argued to be caused by highly dispersed Cu^{2+} species [31]. While its maximum is located above 700 nm for Cu/Ce ratios of 1/2 and 1/4, the band shifts to smaller wavelengths upon a further decrease of the Cu content. This shift has been explained before by quantum confinement effects due to the smaller CuO particle size [31,32]. The spectrum of CuCe(1/1)/SHS is intermediate to those of samples with higher and lower Cu content, showing features of dispersed CuO and bulk CuO. All spectra, with the exception of the one of CuO/SHS, contain a band around 467 nm. This band has earlier been assigned to Cu^{1+} ions in three dimensional clusters of CuO [30]. It is also present in some of the UV–vis spectra of CuO supported by CeO₂ nanorods and polyhedra (but not by ceria cubes) [29]. Unfortunately, Dong et al. did not discuss this prominent feature in their spectra. We tentatively attribute this signal to partially reduced Cu in strong interaction with ceria. The existence of partial reduced copper species on CuO–CeO₂ catalysts has been reported by other groups [33,34]. They proposed that the strong interaction of the copper oxide clusters and cerium oxide [33] or the substitution at the interface of the two oxide phases [34] causes the formation of partial reduced copper species. As ceria contains high concentration of oxygen vacancies based on Raman results, it is not unreasonable to propose that the associated Ce^{3+} would reduce Cu^{2+} ions to Cu⁺. Such a redox reaction has also been suggested by Dong et al. following their observation of reduced Cu by XPS measurements [29].

Fig. 6 displays the H₂-TPR profiles normalized to the Cu content for the CuCe(x)/SHS samples. The H₂ consumption values are collected in Table 2. The values are expressed as the fraction of CuO that could be reduced to metallic Cu using the amount of H₂ consumed. For comparison, Fig. 6 also contains the profiles of CeO₂/SHS and CuO/SHS. The pattern for CeO₂/SHS shows a H₂ consumption feature around 550 °C due to the reduction of the ceria surface, a H₂ production feature at higher temperature due to hydrogen desorption and the onset of bulk ceria reduction around 750 °C [12]. The reduction of the large CuO crystallites in CuO/SHS occurs around 290 °C (γ peak) in line with the reduction temperature of bulk CuO [35]. The samples with a relatively high Cu content exhibit a strong high temperature feature due to bulk CuO reduction. With decreasing Cu/Ce ratio, it is observed that the high temperature peak decreases in intensity and shifts to lower temperature. It follows that the amount and crystallite size of bulk CuO decreases. Simultaneously, a peak appears with a maximum around 230 °C (β peak), which is most pronounced around Cu/Ce = 1. With a further decrease of the Cu/Ce ratio, this peak decreases again and a new reduction feature below 200 °C (α peak) becomes evident. This feature is already present as a weak shoulder in the profile of CuCe(1/1)/SHS. For CuCe(1/2)/SHS and CuCe(1/4)/SHS, all three features are observed. A further decrease of the Cu/Ce ratio leads to considerable changes in the TPR profiles. The low temperature peak becomes increasingly weaker and shifts to higher temperature. The two other peaks at higher temperatures have disappeared and, instead, a broad feature is observed at higher temperature. This feature also broadens and shifts to higher temperature with decreasing Cu/Ce ratio.

Based on literature [9,10,13,29,36,37], we assign the feature below 200 °C to finely dispersed CuO strongly interacting with the ceria surface, the feature between 200 and 250 °C to Cu ions in a solid solution with ceria and also larger CuO particles interacting with the ceria and, as already indicated above, the high temperature feature to bulk CuO. It should also be noted that the amount of H₂ consumed during TPR is higher than the amount of CuO, which is the result of reduction of the ceria surface. This is evident from H₂-TPR for the samples with Cu/Ce < 1, but also for the samples containing more Cu as follows from the Ce 3d XP spectra (vide infra).

Thus, for CuCe(1/32)/SHS, the first reduction feature around 250 °C is due to the reduction of Cu ions in solid solution with the ceria. This sample also contains a small fraction of finely dispersed

Table 2
Catalytic activity of CuCe(x)/SHS in (preferential) CO oxidation.

Catalyst	Reduction degree CuO[a]	Rate$_{CO\,ox}$ [b] CO μmol/g$_{CuO}$ s	Rate$_{PROX}$ [c] CO μmol/g$_{CuO}$/s
CuCe(8/1)/SHS	0.8	1.0	0.6
CuCe(4/1)/SHS	0.9	2.7	2.9
CuCe(2/1)/SHS	1.0	8.8	9.4
CuCe(1/1)/SHS	1.0	8.2	8.9
CuCe(1/2)/SHS	1.1	34.8	39
CuCe(1/4)/SHS	1.3 (1.7)	94 (53)	98 (50)
CuCe(1/8)/SHS	1.6 (2.0)	111 (37)	118 (32)
CuCe(1/16)/SHS	1.9	95	84
CuCe(1/32)/SHS	2.4	35	18
CuCe(1/4)/SHS-IMG	1.3 (1.6)	45 (42)	45 (40)

[a] Fraction of CuO reduced to Cu metal computed from H_2 TPR from room temperature to 600 °C.
[b] CO oxidation conditions: 1 vol% CO and 1 vol% O_2 in He, 40 mL/min, 100 °C; values between brackets after HNO_3 treatment.
[c] PROX conditions: 1 vol% CO, 1 vol% O_2 and 50 vol% H_2 in He, 40 mL/min, 100 °C; values between brackets after HNO_3 treatment.

CuO as evidenced by the UV–vis spectra. Its reduction may be limited because it is already partially reduced. The high temperature reduction peak is likely due to the reduction of the ceria surface. The reason that it extends over a large temperature range is due to the relative higher uncovered surface areas of ceria at low Cu contents. In CuCe(1/16)/SHS, the same two Cu species exist. The UV–vis band around 650 nm supports the presence of small CuO particles. The decrease of the first reduction peak is likely due to the somewhat larger size of the latter particles, as evidenced by the red shift of the characteristic UV–vis band. The increase of the Cu content in CuCe(1/8)/SHS leads to a further increase of the particle size of CuO species and, consequently, their easier reduction as observed from the decrease of the temperature of the first reduction peak. In CuCe(1/4)/SHS, the first reduction peak at 180 °C is due to finely dispersed CuO and the second one around 220–230 °C should have two origins, namely Cu ions in solid solution and larger CuO particles interacting with the ceria. The use of nitric acid to selectively dissolve bulk and small CuO has been reported [6,24,38]. To facilitate the identification of Cu species, CuCe(1/4)/SHS, CuCe(1/4)/SHS-IMG and CuCe(1/8)/SHS were treated with HNO_3. We infer that the second reduction peak is dominated by Cu ions in solid solution with ceria, because removal of CuO clusters/particles by HNO_3 treatment leads to a minor decrease of the second peak, whereas the first one totally disappears (Fig. 7). Indeed, the H_2/CuO ratios are 1.3 and 1.7, respectively, before and after HNO_3 treatment (Table 2). This also confirms that part of the H_2 is used to reduce the ceria surface. The trend is similar for CuCe(1/8)/SHS. In both cases, the reduction extends to higher temperatures, which should be due to the more difficult reduction of the ceria surface as a consequence of the removal of the highly dispersed CuO species. The observation of a rather large and well-defined second reduction feature is likely the result of the uniformity of the highly dispersed Cu ions in the solid ceria solution, which facilitate the reduction of the ceria surface. Therefore, it is not possible to deduce the exact amount of Cu in solid solution from these data. A further increase of the Cu/Ce ratio leads to extensive agglomeration into bulk CuO mainly interacting with the silica support. Although the features of the more dispersed forms of CuO with ceria are not observed anymore because of the strong reduction feature of bulk CuO, such species may still be present in lower relative amount. In contrast to the melt infiltration method, CuCe(1/4)/SHS-IMG exhibits a broader reduction feature (Fig. 7). This sample appears to contain a smaller amount of highly dispersed CuO species, which may indicate that this preparation method leads to a less favorable dispersion. HNO_3 treatment also removed the highly dispersed CuO species and the occurrence of a second broader feature at higher temperature.

The Cu 2p and Ce 3d envelopes of the XP spectra of the CuCe(x)/SHS samples are shown in Fig. 8. The Cu $2p_{3/2}$ binding energy at 933.4 eV and the shake-up peak at 942.7 eV for CuCe(8/1)/SHS point to the predominant presence of CuO [39,40]. With decreasing Cu content, the intensities of the peaks related to Cu decrease. The Cu $2p_{3/2}$ binding energy shifts to lower binding energies (932.5 eV). This shift is accompanied by the disappearance of the shake-up peak. These changes are characteristic for the presence of partially reduced copper species [39]. Because the binding energies of Cu^0 and CuO are within the measurement uncertainty, it is not possible to distinguish between these two oxidation states based on Cu $2p_{3/2}$ photoelectron spectra. An attempt to determine the Auger parameters was not successful, because the Cu LMM $L_3M_{4,5}M_{4,5}$ Auger transition is overlapped by the strong O 1s shake-up peak. The existence of partially reduced copper species in CuO/CeO_2 catalysts has also been reported by other groups and is argued to be due to the strong interaction of copper clusters with cerium oxide [33] or to the substitutions at their interface [34]. It should be noted that quantitative analysis of the Cu oxidation state would in any case be hampered by self-reduction phenomena as a result of exposure to the X-rays. The Ce 3d peaks do not show any shift for the CuCe(x)/SHS samples [41]. The change of the Ce
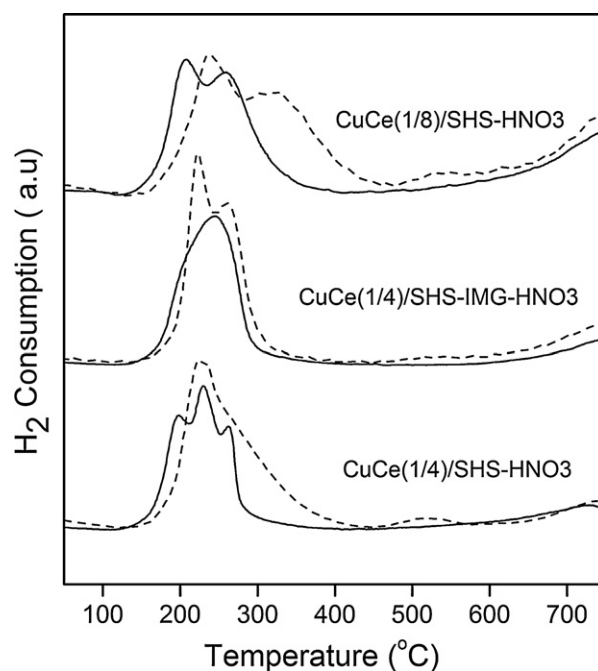
Fig. 7. TPR profiles of CuCe(1/4)/SHS, CuCe(1/4)/SHS-IMG and CuCe(1/8)/SHS after HNO_3 treatment. For comparison, the corresponding parent TPR profiles (solid curves) are included.
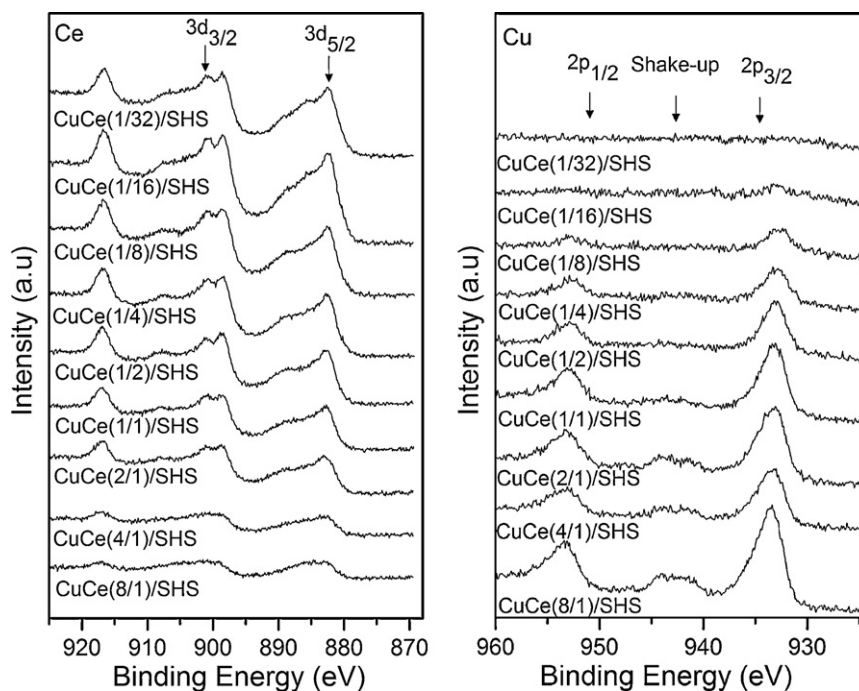
Fig. 8. Cu 2p (left panel) and Ce 3d (right panel) XP spectra of CuCe(x)/SHS catalysts.

$3d_{5/2}$ peak points to an increasing degree of reduction of ceria with increasing Cu/Ce ratio.

In Table 1, the Cu/Ce ratios as determined by XPS analysis are compared to the bulk ICP ratios. At relatively high Cu content, the XPS Cu/Ce ratios are smaller than the bulk ratios. This can be understood in terms of small ceria particles covering the CuO bulk crystallites. It is in agreement with the above finding that at high Cu/Ce ratios the CuO phase mainly interacts with silica. For low Cu/Ce ratios, it is conversely found that the XPS ratios are higher than the corresponding bulk atomic ratios. The difference is largest for CuCe(1/8)/SHS. Thus, in this compositional regime, the morphology may be described in terms of CuO particles dispersed on the surface of CeO_2. The decreasing difference for very low Cu/Ce bulk ratios should be due to an increasing proportion of Cu being part of the $Ce_{1-x}Cu_xO_2$ solid solution. It is furthermore interesting to note that the HNO_3 treatment removes about half of the Cu from CuCe(1/4)/SHS. As the XPS and bulk Cu/Ce ratios are much more similar after acid treatment, it is reasonable to assume that most of the remaining Cu is highly dispersed in the ceria, *i.e.* it is part of the $Ce_{1-x}Cu_xO_2$ solid solution. By comparison to corresponding results for CuCe(1/8)/SHS, it can be concluded that a larger proportion of Cu is in the highly dispersed CuO particles for this sample. From comparison of the results for CuCe(1/4)/SHS to those for CuCe(1/4)/SHS-IMG, it follows that the former samples contains a higher proportion of CuO clusters on the surface in agreement with the TPR results.

In summary, the Cu speciation can be effectively modified by changing the ratio of Cu and Ce salts used in the melt infiltration in the silica hollow sphere support. The extensive characterization did not evidence the formation of metal silicate species during the melt infiltration step. At high Cu/Ce ratio copper is predominantly present as large CuO crystallites as follows from XRD, UV–vis spectroscopy and H_2 TPR measurements. Whereas at high Cu/Ce ratio there is little interaction between CuO and CeO_2, the speciation shifts to smaller CuO particles dispersed over the ceria surface with decreasing Cu/Ce ratio, and at low Cu/Ce ratio, the amount of $Cu_xCe_{1-x}O_2$ solid solution dominates. The UV–vis spectra evidence the presence of partially reduced Cu species, most likely Cu^+.

Careful analysis of the XP spectra points to the presence of Cu^+ species in the samples with lower Cu content. The presence of a solid solution of Cu^{2+} in CeO_2 is also inferred from the Raman spectra. The density of oxygen vacancies in ceria increases with Cu/Ce ratio as a result of the decreasing ceria particle size. It is inferred that at intermediate Cu/Ce ratios the contribution of highly dispersed, partially reduced copper oxide particles is maximum. A decrease of the Cu/Ce ratio will lead to the predominance of Cu in the solid solution.

3.2. Catalytic measurement of CuCe(x)/SHS catalysts

These samples were tested for their catalytic activity in the oxidation of CO as a function of temperature. It can be seen from Fig. 9 that the bimetallic CuCe catalysts exhibit much higher activity
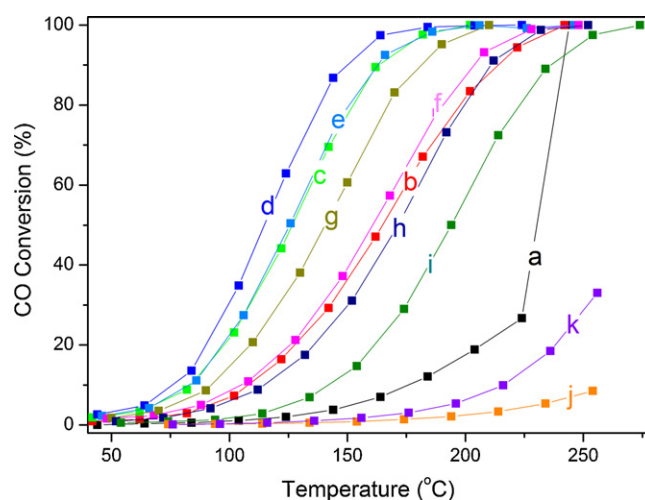

Fig. 9. CO oxidation of CuCe(x)/SHS catalysts as a function of temperature. (a) CuCe(1/32)/SHS, (b) CuCe(1/16)/SHS, (c) CuCe(1/8)/SHS, (d) CuCe(1/4)/SHS, (e) CuCe(1/2)/SHS, (f) CuCe(1/1)/SHS, (g) CuCe(2/1)/SHS, (h) CuCe(4/1)/SHS, (i) CuCe(8/1)/SHS, (j) CeO_2/SHS and (k) CuO/SHS.

than the CuO/SHS and CeO$_2$/SHS references. The catalytic activities of the catalysts at a reaction temperature of 100 °C were normalized on the CuO content. The normalized activity of CuCe(8/1)/SHS is almost four times higher than that of CuO/SHS. The values are collected in Table 2. The increase of the Ce content for large CuO crystallites going from CuCe(8/1)/SHS to CuCe(2/1)/SHS results in an 8-fold increase of the reaction rate. With the appearance of small CuO particles on ceria, the catalytic activities strongly increase. The maximum catalytic activity is obtained for CuCe(1/8)/SHS and it is more than two orders of magnitude higher than the activity of CuCe(8/1)/SHS. A further increase of the Cu/Ce ratio results in a decrease of the activity. From these data, it is clear that the high catalytic activity in CO oxidation is due to the presence of highly dispersed CuO particles on the ceria support. Such conclusion is close to the results reported by Luo et al. [24]. The bulk CuO crystallites in CuCe(8/1)/SHS are more active than the CuO crystallites of CuO/SHS due to the presence of dispersed ceria particles on their surface. The activity is highest for the sample which contains the highest proportion of highly dispersed CuO particles on ceria. The lower activity of the catalysts with a lower Cu/Ce ratio should therefore be due to a decrease of the density of these dispersed CuO particles. The characterization has asserted that Cu is predominantly present in a solid solution with ceria in CuCe(1/32). To verify this, we determined the activities of the acid-treated samples. It is found after acid treatment that (i) the activities of the most active catalysts, CuCe(1/4)/SHS and CuCe(1/8)/SHS decrease significantly and (ii) their normalized activities are similar to that of CuCe(1/32)/SHS. In contrast, it is observed that the normalized activity of the parent and acid-treated CuCe(1/4)/SHS-IMG are very close, which is due to the predominance of Cu in the ceria solid solution. It is instructive to note that the activities of the acid-treated samples as well as CuCe(1/4)/SHS-IMG are quite similar, suggesting that it corresponds to the intrinsic activity of Cu in the Ce$_{1-x}$Cu$_x$O$_2$ solution. By use of this value and the fraction of Cu in the solid solution estimated from the bulk Cu/Ce ratio for CuCe(1/8)/SHS, we estimate a normalized rate for dispersed CuO particles of about 200 μmol/g$_{CuO}$ s. This value is higher than that of CuCe(1/4)/SHS, which is about 132 μmol/g$_{CuO}$ s, due to the smaller CuO particles based on the XRD and UV–vis results.

As already discussed, conventional impregnation preparation of CuCe(1/4)/SHS-IMG results in the predominant presence of Cu in solid solution with ceria. A possible explanation may be that the Cu and Ce nitrate salts are better mixed in the precursor phase of this sample than in the corresponding sample prepared by melt infiltration. Thus, in this particular case, the less efficient mixing of the two components in the precursor leads to a higher proportion of the highly dispersed CuO particles on ceria desired for high CO oxidation activity.

Finally, the performance of these catalysts was evaluated for the preferential oxidation of CO in the presence of H$_2$ as relevant for the cleanup of reformate streams for PEM fuel cell applications. The trend in the activities as a function of temperature is similar to those for CO oxidation as can be seen from Table 2. The activity and selectivity of a subset of these catalysts as a function of temperature are given in Fig. 10. A CO$_2$ selectivity of 100% implies that no H$_2$ was combusted under the given conditions. At low temperatures the CO$_2$ selectivity is 100% except for CuCe(1/32)/SHS. Combustion of hydrogen starts at a higher reaction temperature for CuCe(1/8)/SHS than for CuCe(8/1)/SHS. It was reported that CO oxidation takes place at interfacial positions of the dispersed copper oxide entities with ceria, while H$_2$ oxidation proceeds on partially reduced dispersed copper oxide nanoparticles [14]. This is in line with our observations. Characterization of CuCe(1/8)/SHS points to the presence of partially reduced copper at the interface of the copper and ceria, important to CO oxidation. On the other hand, for CuCe(8/1)/SHS, the existence of such partially reduced copper
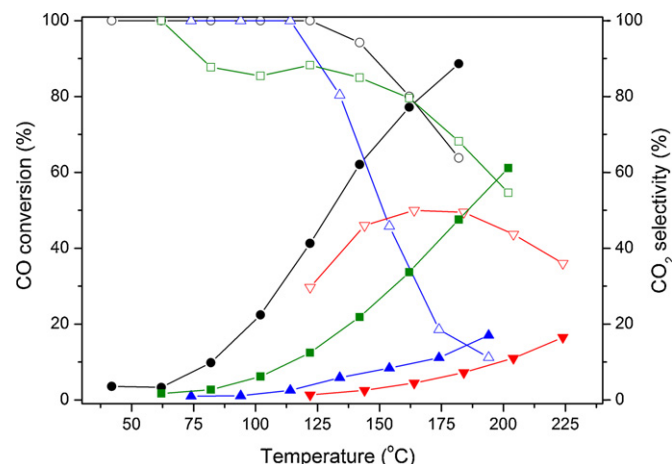

Fig. 10. Preferential oxidation of CO in excess H$_2$ as a function of temperature. Conversion of CO (closed symbols) and selectivity to CO$_2$ (open symbols) for (▼) CuCe(1/32)/SHS, (■) CuCe(1/16)/SHS, (●) CuCe(1/8)/SHS and (▲) CuCe(8/1)/SHS.

species should be dominant on the copper oxide particles themselves. As a result, CuCe(1/8)/SHS shows a higher selectivity to CO$_2$ compared to CuCe(8/1)/SHS. CuCe(1/16)/SHS and CuCe(1/32)/SHS behave quite similarly but different from CuCe(1/8)/SHS. The selectivity is much lower, especially for CuCe(1/32)/SHS. The latter sample is likely a solid solution of Cu in ceria, whereas the former also contains some highly dispersed CuO clusters. It should be further noted that the PROX activities are higher than those in CO oxidation for the CuCe(*x*)/SHS samples going from 8/1 to 1/8, while the trend is reversed for the two samples with a lower Cu/Ce ratio (Table 2). After acid treatment, the trend for CuCe(1/4)/SHS and CuCe(1/8)/SHS becomes different, since in these cases the PROX activity is lower than CO oxidation activity (Table 2). Besides, CuCe(1/4)/SHS-IMG shows comparable activities in the presence and absence of H$_2$. These observations strongly indicate that the solid solution has a higher intrinsic activity towards H$_2$ oxidation. It provides a reasonable explanation for the lower CO$_2$ selectivity of CuCe(1/16)/SHS and CuCe(1/32)/SHS in PROX. Finally, we studied the stability of CuCe(1/4)/SHS at 180 °C under PROX conditions. After an initial deactivation from 96% to 93% observed in the first 6 h time on stream, the activity remained stable for 12 h. The CO$_2$ selectivity increased from 49% to 55% during the initial deactivation period and was stable during the remaining test.

4. Conclusions

The melt infiltration method has been applied for the first time to prepare copper cerium oxide catalysts on silica hollow spheres. These catalysts show enhanced activity in (preferential) CO oxidation to catalyst prepared by solution impregnation method. The proportion of different copper species was varied through variations in the Cu/Ce ratio. At very high Cu/Ce ratio, bulk CuO particles are obtained with low activity for CO oxidation. With decreasing Cu/Ce ratio, the speciation shifts from CuO bulk agglomerates to increasingly dispersed CuO particles dispersed over the ceria part of the composite. The maximum proportion of finely dispersed CuO clusters on CeO$_2$, which display the highest activity in CO oxidation, was observed at a Cu/Ce ratio of 1/8. At very low Cu/Ce ratios, a solid solution of Cu^{2+} in ceria is obtained with a low catalytic performance in the PROX reaction. Conventional co-impregnation already leads to such undesired solid solution at intermediate Cu/Ce ratios. With melt infiltration the segregation of CuO and CeO$_2$ can be obtained in a single step preparation leading to highly active catalysts for preferential CO oxidation.

Acknowledgements

References

[1] J.A. Schwarz, C. Contescu, A. Contescu, Chemical Reviews 95 (1995) 477–510.
[2] S.T. Wong, H.P. Lin, C.Y. Mou, Applied Catalysis A 198 (2000) 103–114.
[3] F.S. Xiao, S. Zheng, J.M. Sun, R.B. Yu, S.L. Qiu, R.R. Xu, Journal of Catalysis 176 (1998) 474–487.
[4] T.M. Eggenhuisen, J.P. den Breejen, D. Verdoes, P.E. de Jongh, K.P. de Jong, Journal of the American Chemical Society 132 (2010) 18318–18325.
[5] A. Trovarelli, Catalysis Reviews: Science and Engineering 38 (1996) 439–520.
[6] W. Liu, M. Flytzani-Stephanopoulos, Journal of Catalysis 153 (1995) 304–316.
[7] A.N. Il'ichev, A.A. Firsova, V.N. Korchak, Kinetics and Catalysis 47 (2006) 585–592.
[8] I. Lopez, T. Valdes-Solis, G. Marban, International Journal of Hydrogen Energy 33 (2008) 197–205.
[9] G. Avgouropoulos, T. Ioannides, H. Matralis, Applied Catalysis B 56 (2005) 87–93.
[10] J. Astudillo, G. Aguila, F. Diaz, S. Guerrero, P. Araya, Applied Catalysis A 381 (2010) 169–176.
[11] G. Avgouropoulos, T. Ioannides, Applied Catalysis A 244 (2003) 155–167.
[12] M.F. Luo, J.M. Ma, J.Q. Lu, Y.P. Song, Y.J. Wang, Journal of Catalysis 247 (2007), 127–127.
[13] J. Zhu, L.L. Zhang, Y. Deng, B. Liu, L.H. Dong, F. Gao, K.Q. Sun, L. Dong, Y. Chen, Applied Catalysis B 96 (2010) 449–457.
[14] D. Gamarra, C. Belver, M. Fernandez-Garcia, A. Martinez-Arias, Journal of the American Chemical Society 129 (2007) 12064–12065.
[15] M. Jobbagy, F. Marino, B. Schobrod, G. Baronetti, M. Laborde, Chemistry of Materials 18 (2006) 1945–1950.
[16] A. Martinez-Arias, M. Fernandez-Garcia, J. Soria, J.C. Conesa, Journal of Catalysis 182 (1999) 367–377.
[17] A. Hornes, A.B. Hungria, P. Bera, A.L. Camara, M. Fernandez-Garcia, A. Martinez-Arias, L. Barrio, M. Estrella, G. Zhou, J.J. Fonseca, J.C. Hanson, J.A. Rodriguez, Journal of the American Chemical Society 132 (2010) 34–35.
[18] J.T. Tang, J. Liu, P.Y. Wang, H. Zhong, Q.H. Yang, Microporous and Mesoporous Materials 127 (2010) 119–125.
[19] J. Liu, Q.H. Yang, L. Zhang, H.Q. Yang, J.S. Gao, C. Li, Chemistry of Materials 20 (2008) 4268–4275.
[20] W. Yue, W.Z. Zhou, Chemistry of Materials 19 (2007) 2359–2363.
[21] L. Chen, P. Fleming, V. Morris, J.D. Holmes, M.A. Morris, Journal of Physical Chemistry C 114 (2010) 12909–12919.
[22] X.Q. Wang, J.A. Rodriguez, J.C. Hanson, D. Gamarra, A. Martinez-Arias, M. Fernandez-Garcia, Journal of Physical Chemistry B 109 (2005) 19595–19603.
[23] S. Deshpande, S. Patil, S.V. Kuchibhatla, S. Seal, Applied Physics Letters 87 (2005) 133113–133115.
[24] M.F. Luo, Y.P. Song, J.Q. Lu, X.Y. Wang, Z.Y. Pu, Journal of Physical Chemistry C 111 (2007) 12686–12692.
[25] Z.-Y. Pu, X.-S. Liu, A.-P. Jia, Y.-L. Xie, J.-Q. Lu, M.-F. Luo, Journal of Physical Chemistry C 112 (2008) 15045–15051.
[26] D. Gamarra, G. Munuera, A.B. Hungria, M. Fernandez-Garcia, J.C. Conesa, P.A. Midgley, X.Q. Wang, J.C. Hanson, J.A. Rodriguez, A. Martinez-Arias, Journal of Physical Chemistry C 111 (2007) 11026–11038.
[27] B.M. Reddy, G. Thrimurthulu, L. Katta, Y. Yamada, S.-E. Park, Journal of Physical Chemistry C 113 (2009) 15882–15890.
[28] G.W. Graham, W.H. Weber, C.R. Peters, R. Usmen, Journal of Catalysis 130 (1991) 310–313.
[29] L. Liu, Z. Yao, Y. Deng, F. Gao, B. Liu, L. Dong, ChemCatChem 3 (2011) 978–989.
[30] H. Praliaud, S. Mikhailenko, Z. Chajar, M. Primet, Applied Catalysis B 16 (1998) 359–374.
[31] V. Indovina, M. Occhiuzzi, D. Pietrogiacomi, S. Tuti, Journal of Physical Chemistry B 103 (1999) 9967–9977.
[32] M. Yin, C.K. Wu, Y.B. Lou, C. Burda, J.T. Koberstein, Y.M. Zhu, S. O'Brien, Journal of the American Chemical Society 127 (2005) 9506–9511.
[33] W. Liu, M. Flytzani-Stephanopoulos, Journal of Catalysis 153 (1995) 317–332.
[34] S. Hocevar, U.O. Krasovec, B. Orel, A.S. Arico, H. Kim, Applied Catalysis B 28 (2000) 113–125.
[35] K.V.R. Chary, G.V. Sagar, D. Naresh, K.K. Seela, B. Sridhar, Journal of Physical Chemistry B 109 (2005) 9437–9444.
[36] W.J. Shan, W.J. Shen, C. Li, Chemistry of Materials 15 (2003) 4761–4767.
[37] G. Aguila, F. Gracia, P. Araya, Applied Catalysis A 343 (2008) 16–24.
[38] M.F. Luo, Y.J. Zhong, X.X. Yuan, X.M. Zheng, Applied Catalysis A 162 (1997) 121–131.
[39] S. Poulston, P.M. Parlett, P. Stone, M. Bowker, Surface and Interface Analysis 24 (1996) 811–820.
[40] V.K. Kaushik, Spectrochimica Acta Part B 44 (1989) 581–587.
[41] L.M. Qiu, F. Liu, L.Z. Zhao, Y. Ma, J.N. Yao, Applied Surface Science 252 (2006) 4931–4935.